Dark-Matter Detection by LSP Scattering

Pekka Toivanen

Contents

1 Introduction

There is extensive evidence suggesting that majority of the matter in our universe is dark, i.e., it does not interact through electromagnetism. Most of the dark matter is believed to consist of Weakly Interacting Massive Particles (WIMP). The standard model of particle physics does not contain a good candidate for the WIMP, but such a candidate is predicted by supersymmetric theories. This candidate is called the Lightest Supersymmetric Particle (LSP). There is a number of experiments carried out to detect WIMPs. These experiments look for recoil signals in nuclei caused by WIMP scattering.

To be able to predict and interpret the results of the dark-matter detection experiments, knowledge of nuclear structure of the detector material is important. For this purpose, in addition to the experimental data, theoretical calculations must be carried out using some nuclear model, for example the nuclear shell model. Theoretically determined event rates for different nuclei help experimental physicists find more suitable detector materials and distinguish the WIMP-nucleon scattering from other events caused by background radiation.

The nuclear shell model is a microscopic model, which describes the nucleus as a system of interacting nucleons. The analogy between the atomic shell model is clear, although there are certain differences. As the described systems consist of several particles, one must use approximate methods to get results. After the nuclear wave functions have been determined, their quality can be tested by comparing calculated observables, such as electromagnetic transition strengths and moments to experimental ones.

In this assignment, the low lying states of ^{127}I, ^{129}Xe, ^{131}Xe and ^{133}Cs were calculated using the shell model. The xenon isotopes in particular are interesting from the point of view of dark-matter detection, as liquid xenon is used in several detectors. The wave functions were used to calculate magnetic dipole moments and reduced transition probabilities for M1-transitions, both of which are important factors in LSP scattering. In addition, to optimize the calculated magnetic properties, effective gyromagnetic factors were determined through a least squares fit of the calculated dipole moments to experimental data. The results of these calculations are part of a report to be published in Physics Letters B.

2 Dark Matter

2.1 Observational Evidence

According to our current knowledge, visible matter constitutes only a small part of the universe. Majority of the mass is made up of dark matter which interacts either weakly or not at all with electromagnetic radiation and therefore cannot be seen directly. Its presence can, however, be observed through its gravitational effects. Observational evidence of dark matter includes the dynamics of galaxies and galaxy clusters and gravitational lensing effects caused by galaxy clusters.

For spiral galaxies, the rotational speed can be calculated as a function of radius using Newtonian mechanics. For example, the disk of luminous matter in the Milky Way has a radius of about 10 kpc and, according to Newton's laws, outside the disk the rotational speed should be proportional to $r^{-1/2}$. Observational evidence suggests, however, that the speed remains constant up to distances of around 50 kpc. The observed rotation curve can be explained with the assumption that the disk of luminous matter is immersed in a halo of dark matter. Furthermore, measuring the rotational speed at different distances from the centre, it is possible to calculate an estimate for the local dark-matter density. For external galaxies, the rotation curves, and subsequently, the effect of the dark halo can be measured with greater accuracy (See figure 1). [1]

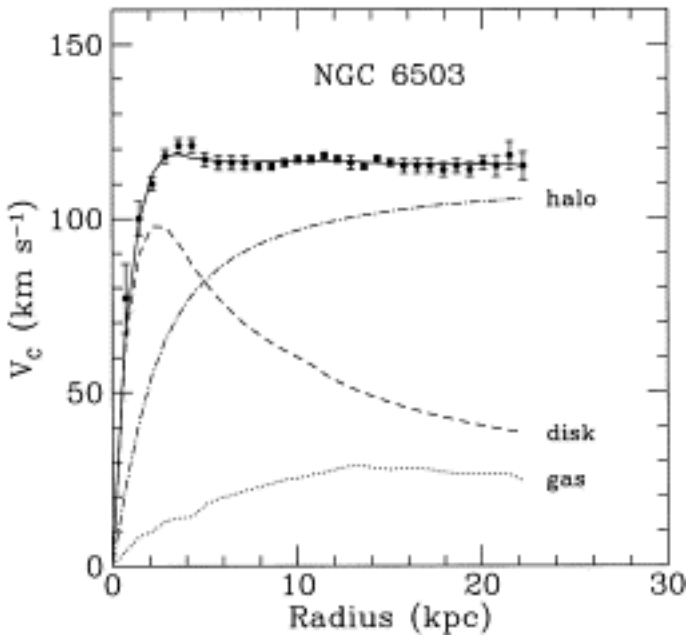

Figure 1: Rotational curve of the spiral galaxy NGC 6503

2.2 Composition

A part of dark matter is believed to consist of so-called MACHOs (Massive Astrophysical Compact Halo Object). These are objects made up of normal baryonic matter emitting little or no electromagnetic radiation. MACHOs may include brown dwarfs, neutron stars and black holes. According to our knowledge of big-bang nucleosynthesis, however, baryonic matter constitutes only a small part of dark matter.

The nonbaryonic component can be further divided into hot and cold dark matter, particles moving at ultra- and nonrelativistic speeds, respectively. The most common candidate for hot dark matter is the neutrino. Structure formation, however, seems to rule out a universe dominated by hot dark matter. To account for the formation of galaxies, it is necessary to assume a dominance of cold dark matter. [2]

In the year 2001 NASA launched the Wilkinson Microwave Anisotropy Probe (WMAP). The purpose of the satellite is to measure temperature fluctuations in the cosmic microwave background radiation (CMB). CMB dates back to the time of recombination, when plasma in the universe had cooled enough to let electrons and protons form neutral atoms, allowing photons to travel freely through space. Combining data from the measurements with cosmological models, it is possible to make estimates of the composition of the universe. The five year results from WMAP yield the following composition: 4.6% baryonic matter, 23% cold dark matter and 72% dark energy [3].

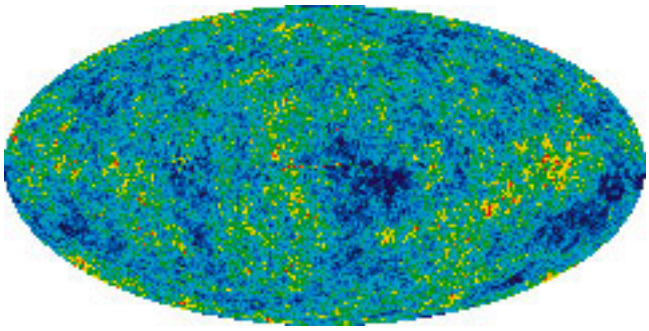

Figure 2: Cosmic microwave background radiation from WMAP five year results

CDM is usually thought to consist of weakly interacting massive particles (WIMP). These are particles that only interact through gravitation and weak interaction. Excluding light particles like neutrinos, the standard model of particle physics does not have a suitable candidate for WIMPs. One is, however, predicted by supersymmetry. According to supersymmetry, every particle in the standard model has a superpartner with a spin that differs by half a unit. This means that for every standard model boson there

exists a supersymmetric fermion. In the minimal supersymmetric standard model two gauginos and two higgsinos (superpartners of gauge and Higgs bosons) mix to form four Majorana mass eigenstates called neutralinos. The lightest of these is stable and is usually the lightest supersymmetric particle (LSP). The predicted abundance of the LSP is typically of order unity, which makes it a good CDM candidate [1].

2.3 Detection

WIMPs interact very weakly with ordinary matter, which makes them extremely difficult to detect. Two main difficulties, in particular, require attention. The nuclear recoil energies in WIMP-nucleon scattering are typically of the order of 10 keV. This means that there is a requirement for very sensitive detectors with low energy thresholds. Another problem arises from the low interaction rate, typically of the order of $10^{-4} \ldots 1$ events/kg/d, depending on SUSY parameters (e.g. mass of the LSP, see figure 3). As a consequence, the WIMP signal is very weak in comparison with the signals from e.g. cosmic background radiation and natural radioactivity. It is therefore necessary to find ways of discriminating the actual LSP scattering from the background.

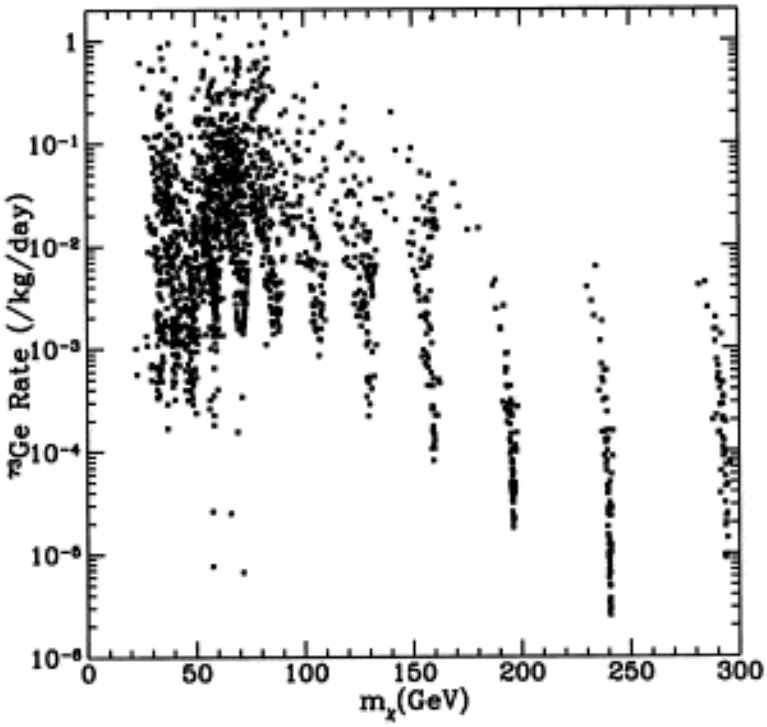

Figure 3: Detection rates for the LSP as a function of its mass in a ^{73}Ge detector for different SUSY parameters [1]

To minimize the amount of cosmic background radiation, experiments are located in underground facilities and protected with extensive shielding to reduce the effect of natural radioactivity (e.g. fast neutrons, gamma rays). Furthermore, redundant detectors are used to eliminate multiple-hit events. Because of the small WIMP-nucleon cross section it is very unlikely that these would be due to WIMPs. In addition, because of the low recoil energies, the detector material must be cooled down to a very low temperature to minimize thermal excitations.

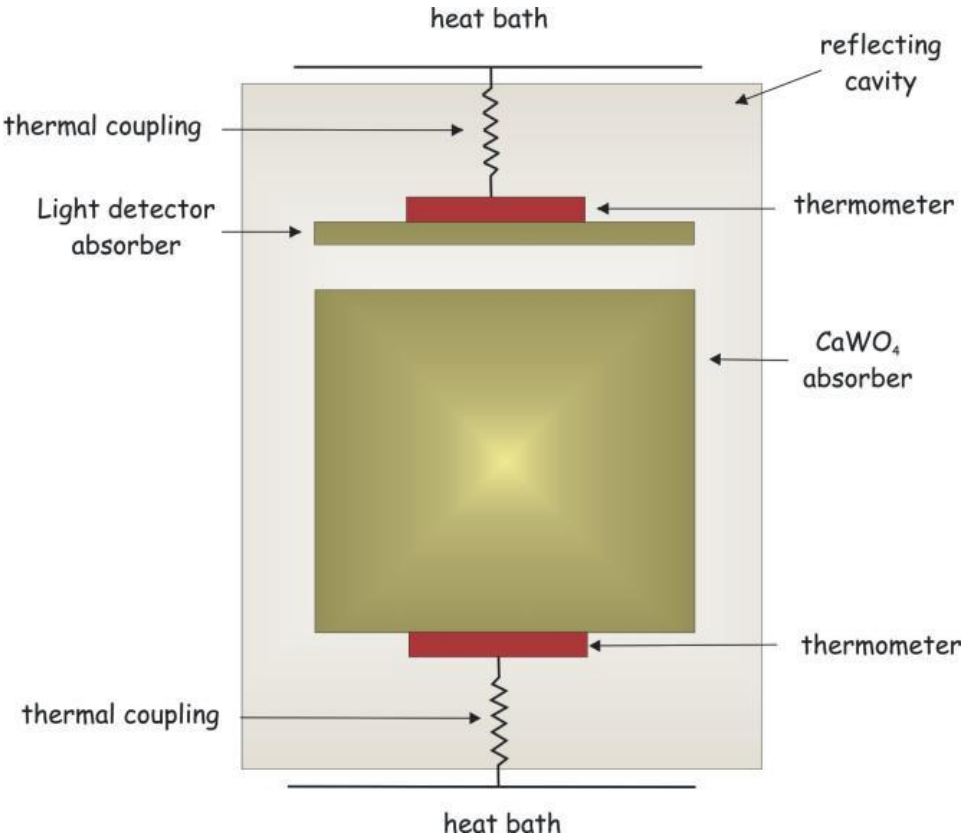

Figure 4: CRESST-II detector

At the moment, there is a number of different experiments to detect WIMPs. For example, the CDMS [4] and EDELWEISS [5] experiments use germanium crystal detectors, with temperatures as low as 10 mK. As the WIMP collides with the detector nuclei, it induces vibrations in the crystal lattice. The heat generated by these phonons can then be measured with great accuracy by, e.g., using a superconductive layer, whose resistance changes dramatically due to a small change in temperature. To further reduce the effect of background radiation, both experiments use another channel to measure ionization in the crystal. Because of the different ioniza-

tion yields for nuclear recoils and gamma radiation, the background can be suppressed by factors larger than 1000. A similar two-channel approach has also been used in the CRESST experiment [6], which uses detectors based on scintillating $CaWO_4$ crystals. For most background radiations, some of the recoil energy is emitted as a scintillation pulse, whereas for the WIMP most of the energy is directed to the phonon channel. Further experiments include the XENON [8] and ZEPLIN [7] projects, which use liquid xenon detectors. Both use simultaneous ionization and scintillation detection to discriminate between nuclear recoils and background electron recoils (See figure 6).

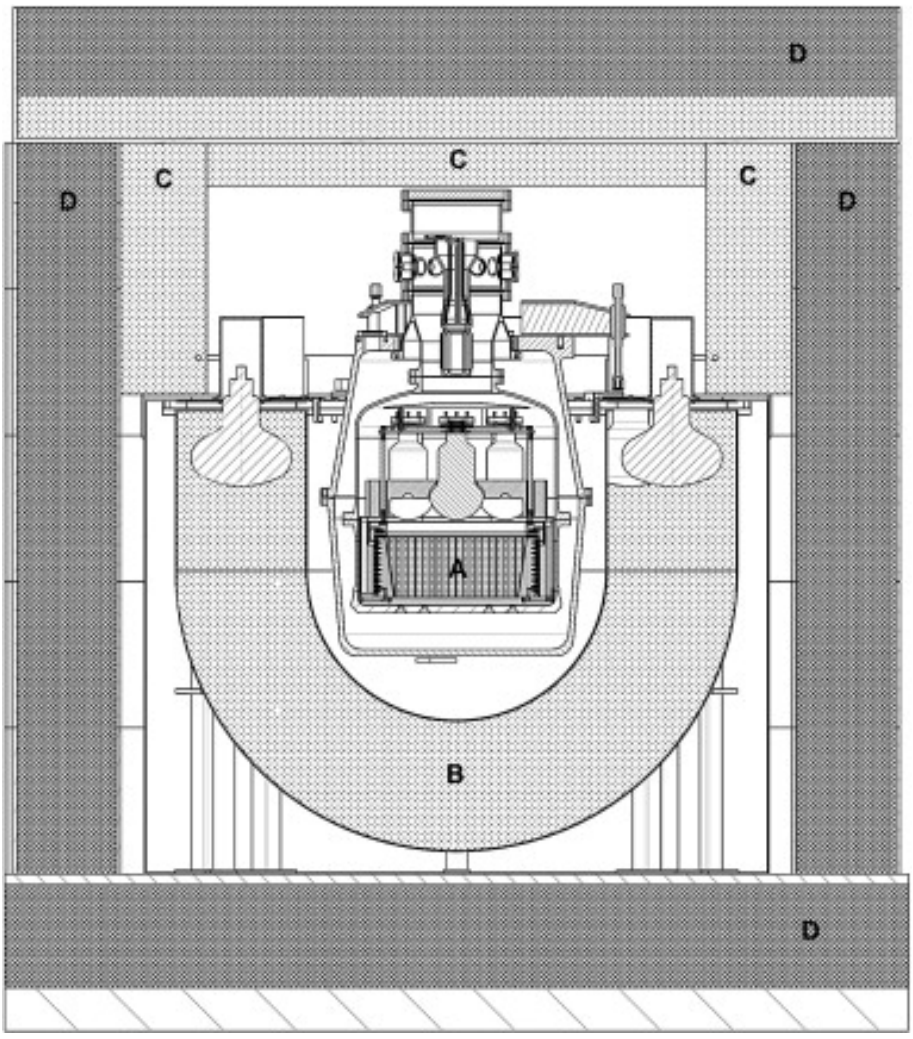

Figure 5: ZEPLIN-II detector: Xe detector (A), liquid scintillator veto (B), Gd-loaded polypropylene hydrocarbon neutron shield (C) and Pb γ-ray shield (D)

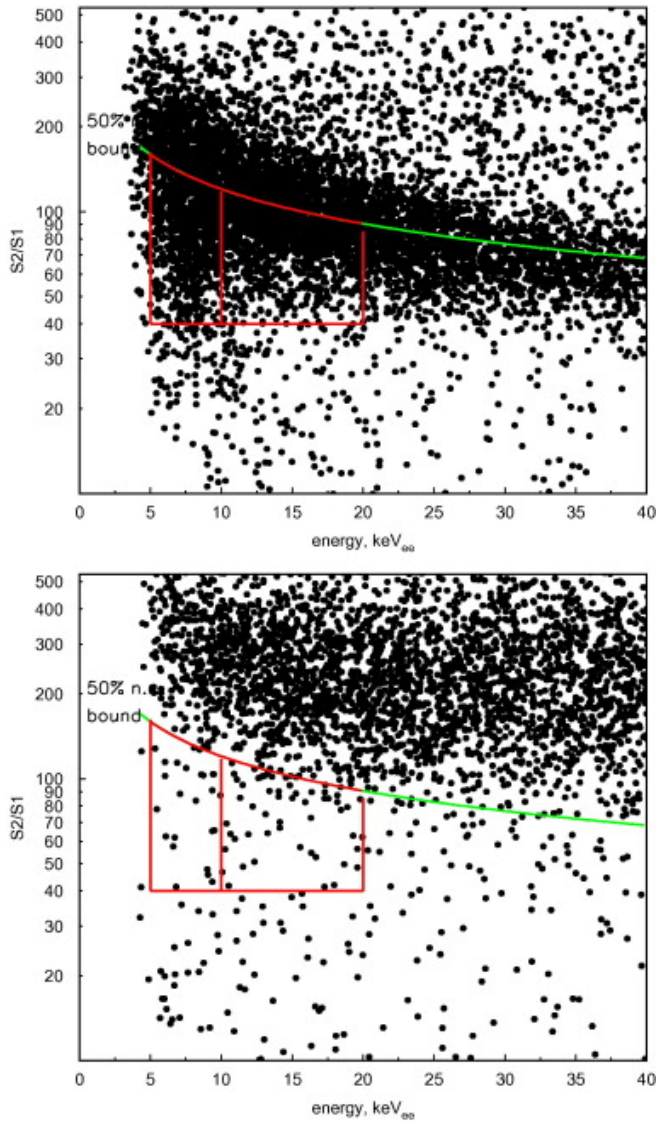

Figure 6: Scintillation to ionization ratio as a function of recoil energy from calibration using neutrons from an AmBe source (upper) and Compton-scattered ^{60}Co γ-rays (lower). Also shown are the 50% nuclear recoil acceptance boundary and the nuclear recoil acceptance window used in the dark matter analysis. [7]

An important characteristic of the WIMP-nucleon scattering is its annual modulation. The event rate depends on the direction of Earth's orbital motion in relation to Sun's movement in the galaxy. There is a peak in the signal around June, when the velocities of Earth and Sun are aligned and the flux passing through Earth is stronger. This modulation can be used to distinguish the WIMP signal from the background (See figure 7).

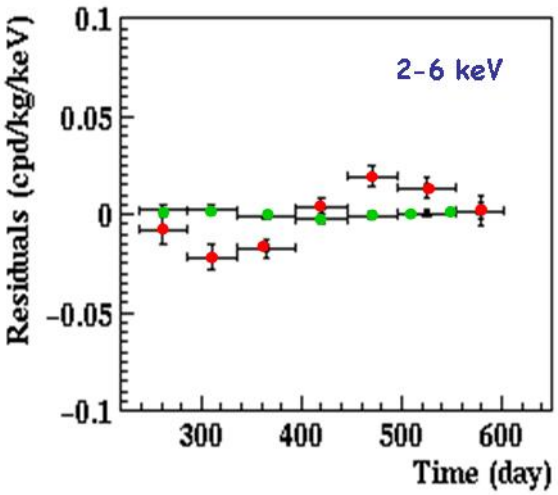

Figure 7: Annual modulation for single-hit and multiple-hit events. A clear modulation can be seen in the single-hit events that include the possible WIMP events. [9]

So far, the only experiment to measure this modulation is the DAMA/NaI [9] experiment, which uses scintillating NaI crystals. The results, however, seem to contradict those of other experiments (See figure 8). Indeed, with further experiments and more stringent limits on the WIMP-nucleon cross section (figure 9), the DAMA result can be ruled out in most SUSY models. Nevertheless, it is possible to reconcile the seemingly contradictory results in some models. For example, the role of spin-dependent and coherent channels has been studied as a possible cause for the discrepancy [10]. Models favouring the spin-dependent channel might be able to explain both results.

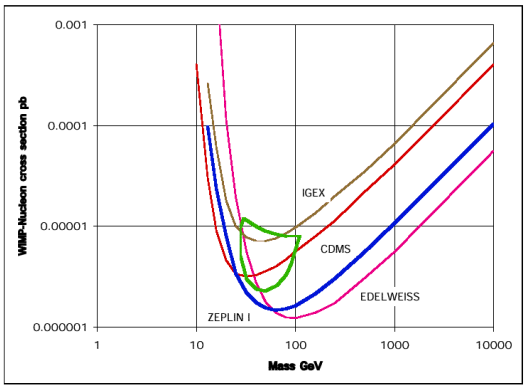

Figure 8: Limits on WIMP-nucleon cross sections from different experiments. The closed contour represents the area of the DAMA result. [11]

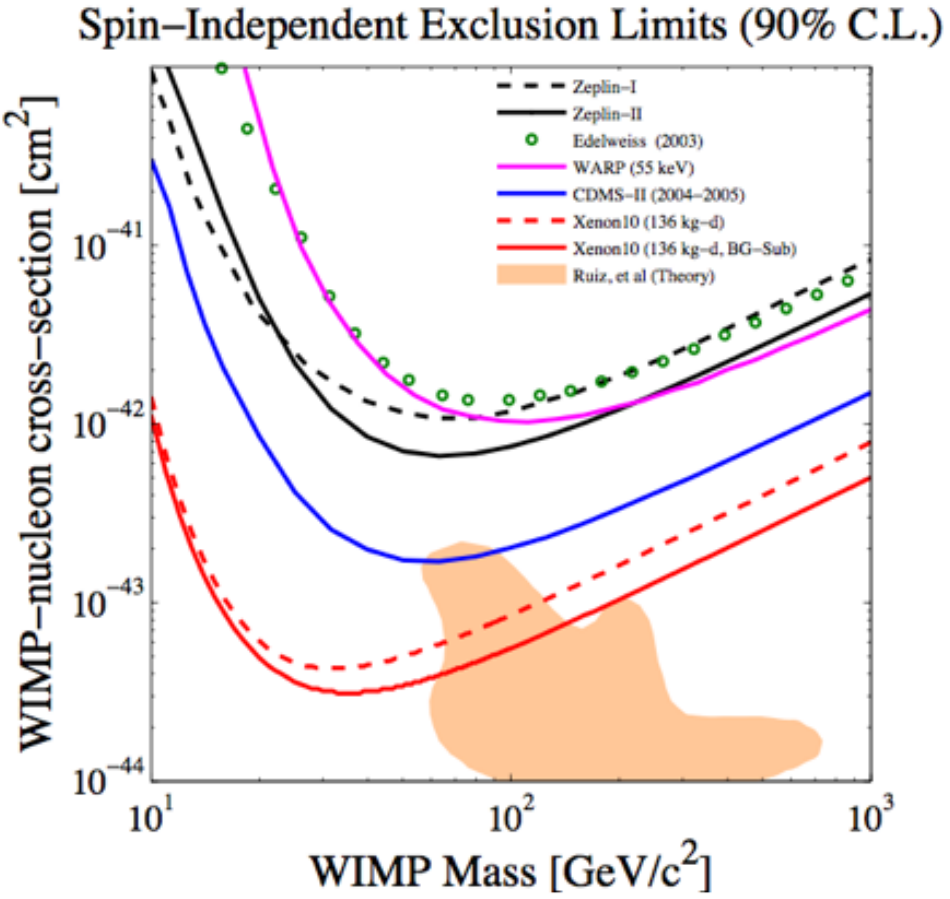

Figure 9: Limits on WIMP-nucleon cross sections from different experiments [8]

2.4 LSP scattering

From the point of view of theoretical physics, the interpretation of the experimental results for the WIMP-nucleon scattering depends on two things. The first is the SUSY model employed to describe the WIMP. The other is the nuclear model describing the structure of the nuclei used in detectors. In order to understand or predict experimental results, calculations have to be carried out for the nuclear properties of the detector material. In this work, the nuclear shell model was used for this purpose. Theoretical calculations can be used to find more efficient detector materials. They also yield information of the expected annual modulation mentioned above.

To calculate average detection rates for a specific nucleus, one must be able to produce the nuclear matrix elements involved in the scattering. In the case of elastic scattering the important state is the ground state. For

inelastic scattering the first excited state must also be calculated. As the relevant matrix elements for LSP scattering depend on spin operators, the nuclear wave functions should reproduce the related data for magnetic dipole moments and M1 transitions in order to be considered reliable.

The event rate for LSP scattering can be written as [10]

$$< R >= [(f_A^0)^2 D_1 + 2 f_A^0 f_A^1 D_2 + (f_A^1)^2 D_3 + A^2 (f_S^0 - f_S^1 \frac{A-2Z}{A}) D_4] m_{det}[kg], \tag{1}$$

where the f coefficients are specific to the employed SUSY model and $m_{det}[kg]$ is the detector mass in units of kg. All the information about the nuclear structure, as well as the dark halo profile, is contained in the coefficients D_n, which are defined as

$$D_1 = \int_{-1}^{+1} \int_{\psi_{min}}^{\psi_{max}} \int_{u_{min}}^{u_{max}} G(\psi, \xi) F_{00}(u) \Omega_0^2 d\xi d\psi du, \tag{2}$$

$$D_2 = \int_{-1}^{+1} \int_{\psi_{min}}^{\psi_{max}} \int_{u_{min}}^{u_{max}} G(\psi, \xi) F_{01}(u) \Omega_0 \Omega_1 d\xi d\psi du, \tag{3}$$

$$D_3 = \int_{-1}^{+1} \int_{\psi_{min}}^{\psi_{max}} \int_{u_{min}}^{u_{max}} G(\psi, \xi) F_{11}(u) \Omega_1^2 d\xi d\psi du, \tag{4}$$

$$D_4 = \int_{-1}^{+1} \int_{\psi_{min}}^{\psi_{max}} \int_{u_{min}}^{u_{max}} G(\psi, \xi) |F(u)|^2 \Omega_0^2 d\xi d\psi du. \tag{5}$$

Here $G(\psi, \xi)$ is a modulation function, $F_{\rho\rho'}(u),\ \rho, \rho' = 0, 1$ are the spin structure functions

$$F_{\rho\rho'}(u) = \sum_{\lambda,\kappa} \frac{\Omega_\rho^{(\lambda,\kappa)}(u) \Omega_{\rho'}^{(\lambda,\kappa)}(u)}{\Omega_\rho \Omega_{\rho'}}, \tag{6}$$

$$\Omega_\rho^{(\lambda,\kappa)}(u) = \sqrt{\frac{4\pi}{2J+1}} (J_f || \sum_{j=1}^{A} [Y_\lambda(\Omega_j) \otimes \sigma(j)]_\kappa j_\lambda(\sqrt{u} r_j) \omega_\rho(j) || J_i), \tag{7}$$

with j_λ a Bessel function, $\omega_0(j) = 1$ and $\omega_1(j) = \tau_3(j)$. $\Omega_\rho = \Omega_\rho^{(0,1)}(0)$ is the static spin matrix element and $F(u)$ the nuclear form factor. For $\psi = v/v_0$ and $u = q^2 b^2/2$, with v the speed of the LSP relative to the detector, v_0 the speed of the sun, q the momentum transfer and b the oscillator parameter, the limits in the integral are different for elastic and inelastic scattering.

3 Nuclear Shell Model

3.1 Eigenenergies and -vectors

The single-particle energy levels of a nucleus form a shell structure resembling that of an atom. Due to some essential differences (e.g. two types of nucleons, the difference between the nuclear and Coulomb interactions) the resulting structure differs from the atomic case (shell closures at different magic particle numbers), but the shell model approach remains, in principle, the most accurate microscopic model for the nucleus.

The nucleus is a many-body system for which an exact solution is usually impossible to obtain and therefore approximate methods, such as perturbation theory, must be applied. In the shell model it is assumed that to a first approximation each nucleon moves independently in an average potential U_i generated by the two-body interactions W_{ik} with the other nucleons. This yields a Hamiltonian of the type

$$\hat{H} = \sum_{i=1}^{A} \hat{T}_i + \sum_{i<k} \hat{W}_{ik} = \sum_{i=1}^{A} (\hat{T}_i + \hat{U}_i) + (\sum_{i<k} \hat{W}_{ik} - \sum_{i=1}^{A} \hat{U}_i) \equiv \hat{H}^0 + \hat{H}^1, \quad (8)$$

where A denotes the number of particles in the nucleus and $\hat{T}_i$ the kinetic-energy operator. $\hat{H}^0$ is the Hamiltonian for independent-particle motion and $\hat{H}^1$ represents a residual two-body interaction. The eigenfunctions for $\hat{H}^0$ can be obtained as Slater determinants

$$|\Phi_{a_1 a_2 \ldots a_A}(1, 2, \ldots, A) >= \frac{1}{\sqrt{A}} \begin{vmatrix} \phi_{a_1}(1) & \phi_{a_1}(2) & \ldots & \phi_{a_1}(A) \\ \phi_{a_2}(1) & \phi_{a_2}(2) & & \vdots \\ \vdots & & \ddots & \vdots \\ \phi_{a_A}(1) & \ldots & \ldots & \phi_{a_A}(A) \end{vmatrix} \quad (9)$$

of single-particle wave functions, i.e. the solutions of the Schrödinger equation

$$(\hat{T} + \hat{U})\phi_a = e_a \phi_a. \quad (10)$$

Here a_i denote the quantum numbers labeling a particular state i and e_a is the single-particle energy. A simple product of single-particle wave functions cannot be used because of the Pauli exclusion principle, which states that for indistinguishable fermions the wave function must be antisymmetric with respect to the interchange of two particle coordinates and spins. On the other hand, since the total angular momentum is conserved, one often uses basis states of definite angular momentum, in which case the Slater determinants alone are not suitable. It is possible, however, to construct an appropriate basis from the Slater determinants using angular-momentum projection operators. Another approach is to use the occupation number formalism [12], which is especially useful when dealing with many particles distributed over

several orbits. For calculations with both protons and neutrons, one can either treat them as distinguishable particles or use the isospin formalism, where they are considered different charge states of the same particle.

For the use of perturbation theory, one tries to determine the average potential U so that the residual interaction becomes small and the true wave function is approximated well by the independent-particle wave function $|\Phi(1,2,\ldots,A)>$. An appropriate potential can be derived through the Hartree-Fock theory [13], but because of the complex nature of the calculations for the corresponding basis, one often starts with a simple single-particle potential such as the harmonic-oscillator or Saxon-Woods potential. Considering the residual interaction as a perturbation, the shifts in the eigenenergies can now be calculated as the expectation value of the interaction in the unperturbed state, i.e. the single-particle state $|\Phi(1,2,\ldots,A)>$. The energy can then be written as

$$E = E^0 + E^1 = \sum_{i=1}^{A} e_{a_i} + < \Phi|\hat{H}^1|\Phi > . \tag{11}$$

In spectroscopic calculations it is usually assumed that the nucleus consists of an inert core of closed shells and N nucleons orbiting it in some prescribed configuration space. Since one is often not interested in the absolute value of energy levels, but rather in the excitation energies and the relative values with respect to the core, it is possible to omit from the Hamiltonian the part dealing solely with the core. If one now assumes that the residual interaction can be described as a two-body interaction, the Hamiltonian can be written as

$$\hat{H} = \sum_{i=1}^{N}(\hat{T}_i + \hat{U}_i) + \sum_{i<k}\hat{V}_{ik} \equiv \hat{H}^0 + \hat{H}^1 \tag{12}$$

and the energy of state $|\Phi(1,2,\ldots,N)>$ as

$$E = \sum_{i=1}^{N} e_{a_i} + < \Phi|\hat{V}|\Phi > \equiv E^0 + E^1. \tag{13}$$

Above, the state $|\Phi(1,2,\ldots,N)>$ represented a pure shell model configuration with a given particle distribution on the single-particle orbitals. One must take into consideration, however, that due to the residual interaction, nucleons may scatter to other states lying close in energy [14]. Assuming there are K such states, the actual states are linear combinations

$$|\Psi_p > = \sum_{k=1}^{K} a_{kp}|\Phi_k >, \qquad p = 1,\ldots,K \tag{14}$$

of these states, for which the Schrödinger equation leads to

$$\sum_{k=1}^{K} H_{lk}a_{kp} \equiv \sum_{k=1}^{K} < \Phi_l|\hat{H}|\Phi_k > a_{kp} = \sum_{k=1}^{K}(E_k^0\delta_{lk} + H_{lk}^1)a_{kp} = E_p a_{lp}, \tag{15}$$

which can be written in matrix form as

$$\begin{pmatrix} H_{11} & H_{12} & \dots & H_{1K} \\ H_{21} & H_{22} & & \vdots \\ \vdots & & \ddots & \vdots \\ H_{K1} & \dots & \dots & H_{KK} \end{pmatrix} \begin{pmatrix} a_{1p} \\ a_{2p} \\ \vdots \\ a_{Kp} \end{pmatrix} = E_p \begin{pmatrix} a_{1p} \\ a_{2p} \\ \vdots \\ a_{Kp} \end{pmatrix}. \tag{16}$$

The eigenenergies and vectors of the Schrödinger equation can now be determined by diagonalizing the matrix H_{lk}. It is clear that for the diagonalization to work, the configuration space must be truncated, as a complete configuration space would lead to matrices of infinite size. One must therefore choose a suitable single-particle model space for the calculations. As a consequence, one must introduce an effective interaction which, acting on the truncated configuration space, yields the same results as the realistic bare interaction in the complete space. It can be shown through the use of the variational principle that the ground state energy in a subset of a given configuration space gives an upper bound for the ground state energy in that space and thus the larger the model space, the better the agreement with the complete configuration space. The size of the model space is of course restricted by the computer used for the calculations.

The many-particle matrix elements $< \Phi_l|V|\Phi_k >$ of the effective interaction can be expressed in terms of single-particle matrix elements through the use of second-quantisation formalism and coefficients of fractional parentage. These elements can then be evaluated in a number of ways. One can obtain the values from experimental data or use certain simple interactions, such as the surface delta potential, which correlate with experimental results [15]. Another approach is to derive the effective interaction from a realistic one. Problems arise because of the repulsive hard core of the realistic interaction, which leads to large or even infinite matrix elements. A solution can be found, however, through the introduction of the Brueckner G-matrix [16], which treats the scattering of the nucleons to intermediate states more accurately and thus removes the infinities from the matrix elements.

For large configuration spaces the size of the Hamiltonian matrix increases rapidly. It is not always necessary, however, to diagonalize the whole matrix. The lower eigenvalues and the corresponding eigenvectors can be obtained with good accuracy through the use of the Lanczos method [17]. The outline of the method is as follows. One first operates with the Hamiltonian on an arbitrarily chosen normalized initial vector $|v_1 >$ in the configuration space, to obtain

$$H|v_1 >= \alpha_1|v_1 > +\beta_1|v_2 >, \tag{17}$$

where $|v_2 >$ is orthogonal to $|v_1 >$. One then operates on $|v_2 >$ to obtain vector $|v_3 >$ orthogonal to $|v_1 >$ and $|v_2 >$. The iteration procedure is continued until a complete set of orthonormal vectors is obtained, which

leads to

$$
\begin{aligned}
&H|v_1>=\alpha_1|v_1>+\beta_1|v_2>,\\
&H|v_2>=\beta_1|v_1>+\alpha_2|v_2>+\beta_2|v_3>,\\
&\quad\vdots\\
&H|v_{K-1}>=\beta_{K-2}|v_{K-2}>+\alpha_{K-1}|v_{K-1}>+\beta_{K-1}|v_K>,\\
&H|v_K>=\beta_{K-1}|v_{K-1}>+\alpha_K|v_K>,
\end{aligned}
\tag{18}
$$

with $\alpha_i =< v_i|H|v_i >$ and $\beta_i =< v_{i+1}|H|v_i >$. In the basis $|v_i >$ the Hamiltonian matrix can now be written in the tridiagonal form

$$
H=\begin{pmatrix}
\alpha_1 & \beta_1 & 0 & \dots & \dots & 0\\
\beta_1 & \alpha_2 & \beta_2 & & & \vdots\\
0 & \beta_2 & \alpha_3 & \beta_3 & & \vdots\\
\vdots & & & \ddots & & \vdots\\
\vdots & & & \beta_{K-2} & \alpha_{K-1} & \beta_{K-1}\\
0 & \dots & \dots & 0 & \beta_{K-1} & \alpha_K
\end{pmatrix}.
\tag{19}
$$

A useful property of this matrix is that the eigenvalues obtained by diagonalizing the upper left $n\times n$ corner of the matrix converge to the eigenvalues of the full matrix. This is especially useful for the determination of the lower eigenvalues, for which the convergence is generally obtained for $n \ll K$.

3.2 Electromagnetic Transitions

Once one has obtained the nuclear wave functions for a given nucleus, a good way to test their quality are the electromagnetic transitions between states. For an electromagnetic multipole operator of rank λ, $\mathcal{M}_{\sigma\lambda\mu}$, the following selection rules apply [18]. Because of the conservation of total angular momentum the matrix elements $< J_fM_f|\mathcal{M}_{\sigma\lambda\mu}|J_iM_i >$ differ from zero only if $|J_i - J_f| \leq \lambda \leq J_i + J_f$. Furthermore, because of the conservation of parity, $\pi_i\pi_f$ must equal $(-1)^\lambda$ for electric transitions ($\sigma = E$), and $(-1)^{\lambda+1}$ for magnetic transitions ($\sigma = M$).

It can be shown that the transition rate from state J_i to J_f is proportional to a measurable quantity known as the reduced transition probability [19]

$$
B(\sigma\lambda; J_i \to J_f) = \frac{(J_f\|\boldsymbol{\mathcal{M}}_{\sigma\lambda}\|J_i)^2}{2J_i+1},
\tag{20}
$$

which is independent of the projection quantum number M. Here we have introduced the reduced matrix element defined by the Wigner-Eckart theorem

$$
< J_fM_f|T_{LM}|J_iM_i >= \frac{(J_iM_iLM|J_fM_f)}{\sqrt{2J_f+1}}(J_f\|\boldsymbol{T}_L\|J_i).
\tag{21}
$$

The matrix element between two many-particle states can be expressed as a linear combination of single-particle matrix elements, which can then be calculated. For two mixed-configuration states

$$|\Psi_i >= \sum_j a_j |\Phi_j >, \qquad |\Psi_f >= \sum_k b_k |\Phi_k >, \tag{22}$$

the reduced matrix element can be calculated from

$$(J_f \| \boldsymbol{\mathcal{M}}_{\sigma\lambda} \| J_i) = \sum_{jk} a_j b_k^* (\Phi_k \| \boldsymbol{\mathcal{M}}_{\sigma\lambda} \| \Phi_j). \tag{23}$$

3.3 Magnetic Dipole Moments

Another important observable quantity for testing the quality of nuclear wave functions is the magnetic dipole moment [20]. In particular, it is relevant for the elastic scattering of WIMPs. The dipole moment is proportional to the transition matrix element

$$\begin{aligned} < JM = J|M_{10}|JM = J > &= \begin{pmatrix} J & 1 & J \\ -J & 0 & J \end{pmatrix} (J \| \boldsymbol{M}_1 \| J) \\ &= \sqrt{\frac{J}{(J+1)(2J+1)}} (J \| \boldsymbol{M}_1 \| J), \end{aligned} \tag{24}$$

where we have used the Wigner-Eckart theorem and the notation $\boldsymbol{M}_\lambda = \boldsymbol{\mathcal{M}}_{M\lambda}$. The conventional magnetic dipole moment is then defined as

$$\frac{\mu}{c} = \sqrt{\frac{4\pi}{3}} \sqrt{\frac{J}{(J+1)(2J+1)}} (J \| \boldsymbol{M}_1 \| J). \tag{25}$$

The magnetic dipole operator can be divided into spin and orbital angular momentum parts, and further into neutron and proton parts. The dipole moment can then be written as

$$\mu = \mu_1 g_s(n) + \mu_2 g_s(p) + \mu_3 g_l(n) + \mu_4 g_l(p), \tag{26}$$

where $g_s(n)$, $g_s(p)$, $g_l(n)$ and $g_l(p)$ are the neutron and proton spin and orbital angular momentum gyromagnetic factors.

3.4 Effective gyromagnetic factors

The magnetic properties of a nucleus are very important for the LSP scattering, so for a reliable calculation the magnetic moments and transitions should be reproduced accurately. For a shell model calculation in a restricted configuration space, effective operators should be used for optimal results. In the case of magnetic operators, one should use effective gyromagnetic factors that yield better results in the configuration space in question. These

can be determined through a least squares fit to experimental data, i.e. by minimizing the function

$$\sum_{k=1}^{n_{data}} [\mu_{k,1} g_s(n) + \mu_{k,2} g_s(p) + \mu_{k,3} g_l(n) + \mu_{k,4} g_l(p) - \mu_{k,exp}]^2. \tag{27}$$

For the minimum, the partial derivatives with respect to gyromagnetic factors vanish, which, denoting the gyromagnetic factors with g_i for $i = 1, 2, 3, 4$, leads to the condition

$$\sum_{k=1}^{n_{data}} (\sum_{i=1}^{4} \mu_{k,i} g_i - \mu_{k,exp}) \mu_{k,j} = 0, \qquad j = 1, 2, 3, 4. \tag{28}$$

This can be written in matrix form as

$$I^T I \vec{g} - I^T \vec{\mu}_{exp} = 0, \tag{29}$$

where I is an $n_{data} \times 4$ matrix with $I_{ki} = \mu_{k,i}$. The gyromagnetic factors can then be determined from the equation

$$\vec{g} = (I^T I)^{-1} I^T \vec{\mu}_{exp}. \tag{30}$$

The fitting procedure in question is a "one-step" operation, where the nuclear wave functions remain constant and only the gyromagnetic factors are varied.

4 Results

The eigenvalues and -vectors of ^{127}I, ^{129}Xe, ^{131}Xe and ^{133}Cs were calculated for $J \leq \frac{11}{2}$ using the shell model program EICODE, which uses angular-momentum projected proton and neutron basis states to calculate the Hamiltonian matrix elements. The effective nucleon-nucleon interactions used were based on the Bonn-CD G-Matrix and folded diagram method by M. Hjorth-Jensen [21]. The calculations were carried out in the $(0g_{7/2} - 1d - 2s - 0h_{11/2})$ valence space with the following restrictions on the configurations: The neutron excitations from the $(0g_{7/2} - 1d_{5/2})$ space were restricted to one in the case of ^{127}I and ^{129}Xe and to two in the case of ^{131}Xe. In addition, an energy centroid restriction was used for ^{129}Xe, ^{131}Xe and ^{133}Cs to exclude configurations with energies above 4.0 MeV. The energy level diagrams are presented in figures 10 and 11 along with the experimental results [22]. Furthermore, results from MQPM calculations [23] for ^{127}I are presented in figure 12 for comparison.

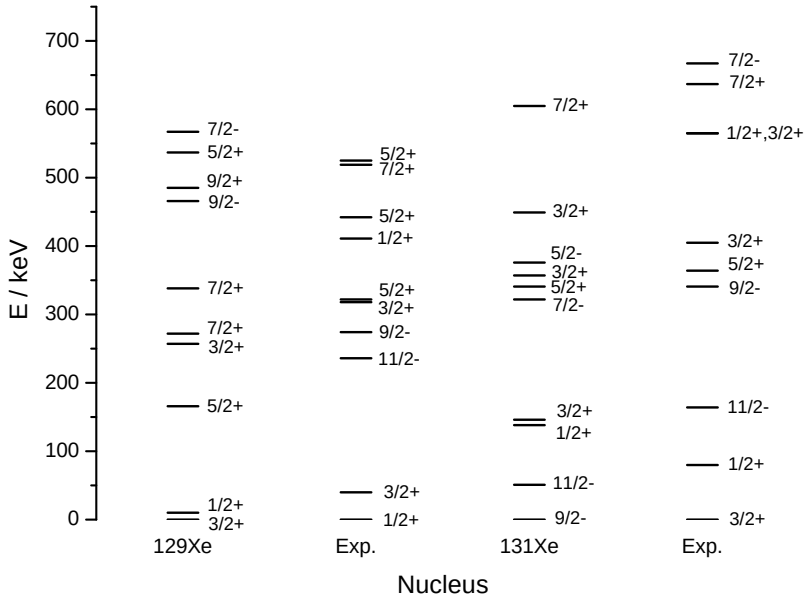

Figure 10: Shell model and experimental energy level diagrams for ^{129}Xe and ^{131}Xe

After the calculation of the nuclear wave functions, the magnetic dipole moments were calculated for the low-lying states in each nucleus. A least squares fit with the experimental results yielded the effective gyromagnetic factors presented in table 1.

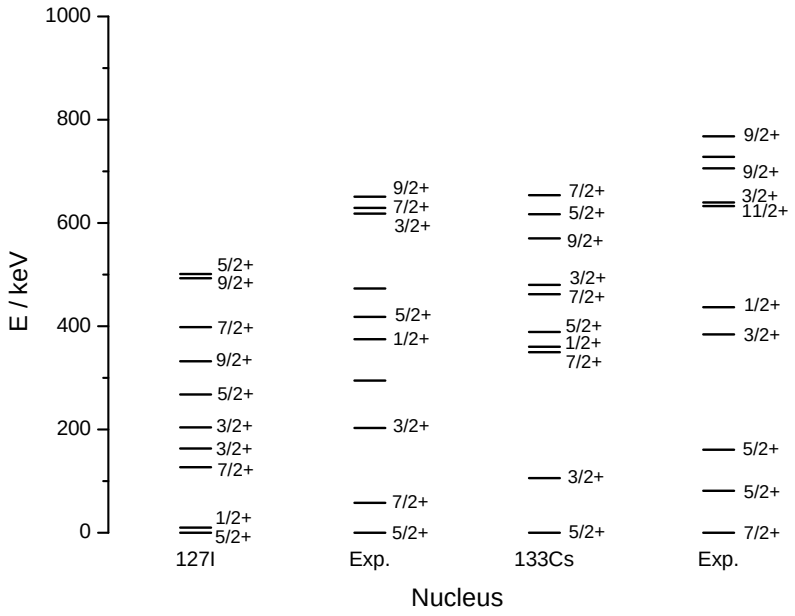

Figure 11: Shell model and experimental energy level diagrams for ^{127}I and ^{133}Cs

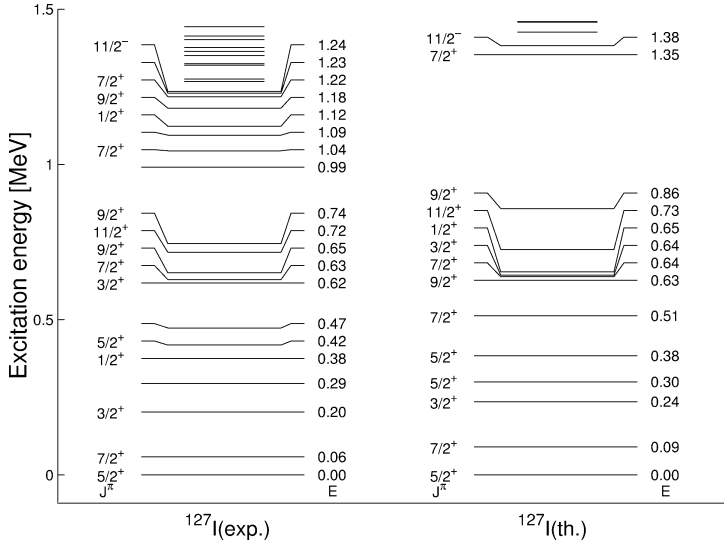

Figure 12: MQPM energy level diagram for ^{127}I

Table 1: Effective gyromagnetic factors from the LLS fit to experimental data

$g_s(n)$	$g_s(p)$	$g_l(n)$	$g_l(p)$
-3.370	3.189	0.0190	1.119

Both the bare and effective values of the dipole moments are tabulated in tables 2, 3, 4 and 5 along with the experimental results [24]. In addition, for the ground state of ^{127}I, results from shell model calculations using two different interactions [25] and from MQPM calculations [26] are tabulated for comparison. Finally, magnetic transitions in the low-lying states were calculated using both bare and effective gyromagnetic factors. These are tabulated in tables 6, 7, 8 and 9 along with the experimental transition strengths [22].

Table 2: Magnetic dipole moments for ^{127}I in units of nuclear magnetons

J^π	Bare	Effective	Experimental	Bonn-A	Nijmegen-II	MQPM
$\frac{5}{2}^+$	3.55	2.74	2.81	2.78	3.15	4.93
$\frac{7}{2}^+$	1.05	2.24	2.54	-	-	-
$\frac{3}{2}^+$	-0.29	0.66	0.97	-	-	-

Table 3: Magnetic dipole moments for ^{129}Xe in units of nuclear magnetons

J^π	Bare	Effective	Experimental
$\frac{1}{2}^+$	-0.94	-0.80	-0.78
$\frac{3}{2}^+$	0.45	0.49	0.58
$\frac{11}{2}^-$	-1.17	-0.81	-0.89

Table 4: Magnetic dipole moments for ^{131}Xe in units of nuclear magnetons

J^π	Bare	Effective	Experimental
$\frac{3}{2}^+$	0.72	0.72	0.69
$\frac{11}{2}^-$	-1.37	-1.01	-0.99

Table 5: Magnetic dipole moments for ^{133}Cs in units of nuclear magnetons

J^π	Bare	Effective	Experimental
$\frac{7}{2}^+$	1.67	2.87	2.58
$\frac{5}{2}^+$	4.03	3.33	3.45
$\frac{5}{2}^+_2$	1.82	2.31	2.00

Table 6: M1-transitions for ^{127}I in units of $(\mu_N/c)^2$

Transition	Bare	Effective	Experimental
$\frac{7}{2}^+ \rightarrow \frac{5}{2}^+$	5.01E-3	8.46E-4	2.20E-2
$\frac{3}{2}^+ \rightarrow \frac{5}{2}^+$	1.28E-1	6.58E-2	7.95E-3
$\frac{1}{2}^+ \rightarrow \frac{3}{2}^+$	7.47E-6	1.58E-4	1.34E-1
$\frac{5}{2}^+_2 \rightarrow \frac{3}{2}^+$	1.31E-1	2.06E-2	3.67E-2
$\frac{5}{2}^+_2 \rightarrow \frac{7}{2}^+$	2.13E-2	6.85E-2	2.72E-2
$\frac{5}{2}^+_2 \rightarrow \frac{5}{2}^+$	7.68E-2	3.58E-2	1.32E-1

Table 7: M1-transitions for ^{129}Xe in units of $(\mu_N/c)^2$

Transition	Bare	Effective	Experimental
$\frac{3}{2}^+ \rightarrow \frac{1}{2}^+$	4.22E-2	3.28E-2	4.92E-2
$\frac{3}{2}^+_2 \rightarrow \frac{3}{2}^+$	1.82E-2	1.06E-2	4.55E-3
$\frac{3}{2}^+_2 \rightarrow \frac{1}{2}^+$	1.20E-3	1.40E-3	9.85E-3
$\frac{5}{2}^+ \rightarrow \frac{3}{2}^+$	1.53E-1	1.15E-1	1.75E-2

Table 8: M1-transitions for ^{131}Xe in units of $(\mu_N/c)^2$

Transition	Bare	Effective	Experimental
$\frac{1}{2}^+ \rightarrow \frac{3}{2}^+$	5.87E-2	4.32E-2	6.20E-2
$\frac{9}{2}^- \rightarrow \frac{11}{2}^-$	1.25E-2	1.24E-2	1.79E-4
$\frac{5}{2}^+ \rightarrow \frac{3}{2}^+$	2.76E-2	1.98E-2	6.62E-4
$\frac{3}{2}^+_2 \rightarrow \frac{1}{2}^+$	6.92E-3	5.15E-3	1.07E-2
$\frac{3}{2}^+_2 \rightarrow \frac{3}{2}^+$	2.02E-2	1.26E-2	1.07E-2

Table 9: M1-transitions for ^{133}Cs in units of $(\mu_N/c)^2$

Transition	Bare	Effective	Experimental
$\frac{5}{2}^+ \rightarrow \frac{7}{2}^+$	2.65E-3	1.39E-4	4.24E-3
$\frac{5}{2}^+_2 \rightarrow \frac{5}{2}^+$	3.83E-2	1.37E-2	1.38E-1
$\frac{5}{2}^+_2 \rightarrow \frac{7}{2}^+$	4.93E-3	6.62E-3	2.09E-3
$\frac{3}{2}^+ \rightarrow \frac{5}{2}^+_2$	1.79E-1	5.46E-2	2.60E-3
$\frac{3}{2}^+ \rightarrow \frac{5}{2}^+$	3.52E-1	1.28E-1	4.30E-2

5 Conclusions

In this report, dark-matter detection and in particular the scattering of the dark-matter candidate LSP was reviewed. Shell model calculations were carried out for the promising detector materials ^{127}I, ^{129}Xe, ^{131}Xe and ^{133}Cs to determine nuclear properties essential for the description of LSP scattering.

For ^{127}I, the two low-lying states whose spins are not known make it slightly difficult to evaluate the results. On the basis of the shell model calculations alone, the first would seem to be a $\frac{3}{2}^+$ state. Comparison with the MQPM calculation suggests, however, that it is a $\frac{5}{2}^+$ state, while the second is a $\frac{7}{2}^+$ state. If this is indeed the case, the lowest states are reproduced quite well apart from the first $\frac{1}{2}^+$ state and the second $\frac{3}{2}^+$ state, which are much too low. The leading proton configuration for both of these states is $[g^2_{7/2}d_{5/2}]_{5/2^+}$, whereas e.g. for the first $\frac{3}{2}^+$ and $\frac{7}{2}^+$ states it is $[g_{7/2}d^2_{5/2}]_{7/2^+}$. This might explain the low energies, since the $g_{7/2}$ orbit is 0.3 MeV below the $d_{5/2}$ orbit.

For ^{133}Cs the spins of the lowest five states (though not their relative order) are predicted correctly, but the overall discrepancy is much larger. For the xenon isotopes, the low-lying $\frac{9}{2}^-$ and $\frac{11}{2}^-$ states seem to be problematic. In ^{129}Xe the calculated negative parity states are too high in energy, while in ^{131}Xe they are too low. The states with lower spin seem to be better in accordance with the experimental results. The first states are in the wrong order, but since the experimental energies are close to each other this is no great concern.

In the bare magnetic dipole moments, there is a clear difference between the neutron odd xenon isotopes and the proton odd nuclei ^{127}I and ^{133}Cs. For the xenon isotopes, the discrepancy with the experimental results is of the order 0.1 μ_N, whereas for ^{127}I and ^{133}Cs it is an order of magnitude larger. This can also be seen in the effective gyromagnetic factors. Since the transition matrix elements (and the dipole moments) in neutron odd nuclei depend heavily on the single-particle matrix elements between neutron states, the corrections to the neutron gyromagnetic factors from the fit are quite small. Similarly, for the proton gyromagnetic factors, larger corrections are required because of the larger discrepancy.

As can be expected, the fitted gyromagnetic factors improve the calculated dipole moments significantly. The situation is different, however, for the M1-transitions which were not used in the fit. There are corrections of up to an order of magnitude in the proton odd nuclei, but the overall agreement with experimental data does not change considerably. For the neutron odd nuclei, the corrections are quite small and no real improvement can be seen. For bare and effective values alike, there are differences of up to two orders of magnitude. Most notably, for the transition in ^{127}I from the first $\frac{1}{2}^+$ state to the first $\frac{3}{2}^+$ state, the bare and effective values differ from

the experimental one by four and three orders of magnitude, respectively. This might be due to the composition of the $\frac{1}{2}^+$ state, since its energy is also much too low.

From the point of view of LSP scattering, the data for the relevant states, i.e. the ground states and the first excited states in the xenon isotopes, is reproduced remarkably well. For the dipole moments, the effective gyromagnetic factors further improve the bare values, which are already quite accurate. For M1 transitions, the bare values are very close to the experimental ones and are actually slightly better than the effective values. Because of the good overall agreement between theoretical and experimental dipole moments, the results can be considered reliable for elastic scattering. The somewhat large errors in some of the transition strengths, however, raise some questions about their validity for inelastic scattering.

References

[1] K. Griest, M. Kamionkowski, Physics Reports 333-334 (2000) 167-182

[2] http://astro.berkeley.edu/ mwhite/darkmatter/hdm.html

[3] http://map.gsfc.nasa.gov/news/index.html

[4] http://cdms.berkeley.edu/

[5] V. Sanglard et al., Phys. Rev. D 71 (2005) 122002

[6] http://www.cresst.de/

[7] G.J. Alner et al., Astroparticle Physics 28 (2007) 287-302

[8] http://xenon.astro.columbia.edu/

[9] http://people.roma2.infn.it/ dama/web/home.html

[10] M. Kortelainen et al., Phys. Lett. B 632 (2006) 226

[11] http://hepwww.rl.ac.uk/ukdmc/results/ZIlimit75d.html

[12] K.L.G. Heyde, *The Nuclear Shell Model* (Springer-Verlag, Berlin Heidelberg) p. 184-194 (1994)

[13] P.J. Brussaard, P.W.M. Glaudemans, *Shell-Model Applications in Nuclear Spectroscopy* (North-Holland Publishing Company, Amsterdam) p. 5-6 (1977)

[14] P.J. Brussaard, P.W.M. Glaudemans, *Shell-Model Applications in Nuclear Spectroscopy* (North-Holland Publishing Company, Amsterdam) p. 52-56 (1977)

[15] K.L.G. Heyde, *The Nuclear Shell Model* (Springer-Verlag, Berlin Heidelberg) p. 81-91 (1994)

[16] M. Hjorth-Jensen, T.T.S. Kuo, E. Osnes, Physics Reports 261 (1995) 130-134

[17] P.J. Brussaard, P.W.M. Glaudemans, *Shell-Model Applications in Nuclear Spectroscopy* (North-Holland Publishing Company, Amsterdam) p. 371-376 (1977)

[18] P.J. Brussaard, P.W.M. Glaudemans, *Shell-Model Applications in Nuclear Spectroscopy* (North-Holland Publishing Company, Amsterdam) p. 187-188 (1977)

[19] P.J. Brussaard, P.W.M. Glaudemans, *Shell-Model Applications in Nuclear Spectroscopy* (North-Holland Publishing Company, Amsterdam) p. 188-189 (1977)

[20] J. Suhonen, *From Nucleons to Nucleus: Concepts of Microscopic Nuclear Theory* (Springer, Berlin) p. 128-130 (2007)

[21] M. Hjorth-Jensen, Private communication

[22] http://ie.lbl.gov/ensdf/

[23] E. Holmlund, J. Suhonen, Nuclear Physics A 706 (2002) 335-350

[24] http://ie.lbl.gov/toipdf/mometbl.pdf

[25] M.T. Ressell, D.J. Dean, Phys. Rev. C 48 (1997) 535

[26] E. Holmlund et al., Phys. Lett. B 584 (2004) 31-39

Appendices

Theoretical and Experimental Energy Levels

Table 10: The first ten energy levels for ^{127}I

Theoretical		Experimental	
J^π	Energy / keV	J^π	Energy / keV
$\frac{5}{2}^+$	0	$\frac{5}{2}^+$	0
$\frac{1}{2}^+$	10	$\frac{7}{2}^+$	58
$\frac{7}{2}^+$	127	$\frac{3}{2}^+$	203
$\frac{3}{2}^+$	163	-	295
$\frac{3}{2}^+$	204	$\frac{1}{2}^+$	375
$\frac{5}{2}^+$	268	$\frac{5}{2}^+$	418
$\frac{9}{2}^+$	332	-	473
$\frac{7}{2}^+$	398	$\frac{3}{2}^+$	618
$\frac{9}{2}^+$	493	$\frac{7}{2}^+$	629
$\frac{5}{2}^+$	501	$\frac{9}{2}^+$	651

Table 11: The first ten energy levels for ^{129}Xe

Theoretical		Experimental	
J^π	Energy / keV	J^π	Energy / keV
$\frac{3}{2}^+$	0	$\frac{1}{2}^+$	0
$\frac{1}{2}^+$	10	$\frac{3}{2}^+$	40
$\frac{5}{2}^+$	166	$\frac{11}{2}^-$	236
$\frac{3}{2}^+$	257	$\frac{9}{2}^-$	274
$\frac{7}{2}^+$	272	$\frac{3}{2}^+$	318
$\frac{7}{2}^+$	338	$\frac{5}{2}^+$	322
$\frac{9}{2}^-$	466	$\frac{1}{2}^+$	411
$\frac{9}{2}^+$	485	$\frac{5}{2}^+$	442
$\frac{5}{2}^+$	537	$\frac{7}{2}^+$	519
$\frac{7}{2}^-$	567	$\frac{5}{2}^+$	525

Table 12: The first ten energy levels for ^{131}Xe

Theoretical		Experimental	
J^π	Energy / keV	J^π	Energy / keV
$\frac{9}{2}^-$	0	$\frac{3}{2}^+$	0
$\frac{11}{2}^-$	51	$\frac{1}{2}^+$	80
$\frac{1}{2}^+$	138	$\frac{11}{2}^-$	164
$\frac{3}{2}^+$	146	$\frac{9}{2}^-$	341
$\frac{7}{2}^-$	322	$\frac{5}{2}^+$	364
$\frac{5}{2}^+$	341	$\frac{3}{2}^+$	405
$\frac{3}{2}^+$	357	$\frac{1}{2}^+$	565
$\frac{5}{2}^-$	376	$\frac{3}{2}^+$	565
$\frac{3}{2}^+$	449	$\frac{7}{2}^+$	637
$\frac{7}{2}^+$	605	$\frac{7}{2}^-$	667

Table 13: The first ten energy levels for ^{133}Cs

Theoretical		Experimental	
J^π	Energy / keV	J^π	Energy / keV
$\frac{5}{2}^+$	0	$\frac{7}{2}^+$	0
$\frac{3}{2}^+$	106	$\frac{5}{2}^+$	81
$\frac{7}{2}^+$	350	$\frac{5}{2}^+$	161
$\frac{1}{2}^+$	360	$\frac{3}{2}^+$	384
$\frac{5}{2}^+$	389	$\frac{1}{2}^+$	437
$\frac{7}{2}^+$	462	$\frac{11}{2}^+$	633
$\frac{3}{2}^+$	480	$\frac{3}{2}^+$	640
$\frac{9}{2}^+$	570	$\frac{9}{2}^+$	706
$\frac{5}{2}^+$	617	-	728
$\frac{7}{2}^+$	654	$\frac{9}{2}^+$	768